



The density structure around quasars from optical depth statistics

Emmanuel Rollinde, Raghunathan Srianand, Tom Theuns, Patrick Petitjean,
Hum Chand

► To cite this version:

Emmanuel Rollinde, Raghunathan Srianand, Tom Theuns, Patrick Petitjean, Hum Chand. The density structure around quasars from optical depth statistics. *Monthly Notices of the Royal Astronomical Society*, 2005, 361, pp.1015-1029. 10.1111/j.1365-2966.2005.08931.x . hal-03786473

HAL Id: hal-03786473

<https://hal.science/hal-03786473>

Submitted on 24 Feb 2023

HAL is a multi-disciplinary open access archive for the deposit and dissemination of scientific research documents, whether they are published or not. The documents may come from teaching and research institutions in France or abroad, or from public or private research centers.

L'archive ouverte pluridisciplinaire **HAL**, est destinée au dépôt et à la diffusion de documents scientifiques de niveau recherche, publiés ou non, émanant des établissements d'enseignement et de recherche français ou étrangers, des laboratoires publics ou privés.

The density structure around quasars from optical depth statistics[★]

Emmanuel Rollinde,^{1†} Raghunathan Srianand,¹ Tom Theuns,^{2,3}
Patrick Petitjean^{4,5} and Hum Chand¹

¹Inter-University Centre for Astronomy and Astrophysics (IUCAA), Post Bag 4, Ganeshkhind, Pune 411 007, India

²Institute for Computational Cosmology, Department of Physics, University of Durham, South Road, Durham DH1 3LE

³University of Antwerp, Campus Drie Eiken, Universiteitsplein 1, B-2610 Antwerp, Belgium

⁴Institut d'Astrophysique de Paris – CNRS, 98bis Boulevard Arago, F-75014 Paris, France

⁵LERMA, Observatoire de Paris, 61 Avenue de l'Observatoire, F-75014, Paris, France

Accepted 2005 May 25. Received 2005 February 14; in original form 2004 October 4

ABSTRACT

We present a method for studying the proximity effect and the density structure around redshift $z = 2\text{--}3$ quasars. It is based on the probability distribution of Lyman α pixel optical depths and its evolution with redshift. We validate the method using mock spectra obtained from hydrodynamical simulations, and then apply it to a sample of 12 bright quasars at redshifts 2–3 observed with the Ultraviolet and Visible Echelle Spectrograph (UVES) at the VLT-UT2 Kueyen European Southern Observatory telescope. These quasars do not show signatures of associated absorption and have a mean monochromatic luminosity of $5.4 \times 10^{31} h^{-2} \text{ erg s}^{-1} \text{ Hz}^{-1}$ at the Lyman limit. The observed distribution of optical depth within $10 h^{-1} \text{ Mpc}$ from the quasi-stellar object is statistically different from that measured in the general intergalactic medium at the same redshift. Such a change will result from the combined effects of the increase in photoionization rate above the mean ultraviolet-background due to the extra ionizing photons from the quasar radiation (proximity effect), and the higher density of the intergalactic medium if the quasars reside in overdense regions (as expected from biased galaxy formation). The first factor decreases the optical depth whereas the second increases the optical depth, but our measurement cannot distinguish a high background from a low overdensity. An overdensity of the order of a few is required if we use the amplitude of the ultraviolet-background inferred from the mean Lyman α opacity. If no overdensity is present, then we require the ultraviolet-background to be higher, and consistent with the existing measurements based on standard analysis of the proximity effect.

Key words: methods: data analysis – methods: N -body simulations – methods: statistical – intergalactic medium – quasars: absorption lines – galaxies: structure.

1 INTRODUCTION

The hydrogen Lyman α absorption lines of the ‘Lyman α forest’ seen in the spectra of distant quasars are a powerful probe of the physical conditions in the intergalactic medium (IGM) at high redshifts ($1.8 \leq z \leq 6$). It is believed that most of the lines with column density, $N_{\text{H I}} \lesssim 10^{14} \text{ cm}^{-2}$ originate in quasi-linear density fluctuations in which the hydrogen gas is in ionization equilibrium with a metagalactic ultraviolet (UV) background produced by star-forming galaxies and quasars. Non-linear effects are unimportant and there-

fore the properties of the Lyman α forest are described well by just three basic ingredients: quasi-linear theory for the growth of baryonic structure, an UV radiation field, and the temperature of the gas (Bi 1993; Muecket et al. 1996; Bi & Davidsen 1997; Hui, Gnedin & Zhang 1997; Weinberg 1999; Choudhury, Srianand & Padmanabhan 2001a; Choudhury, Padmanabhan & Srianand 2001b; Schaye 2001; Viel et al. 2002a). This paradigm is impressively confirmed by full hydrodynamical simulations (Cen et al. 1994; Zhang, Anninos & Norman 1995; Miralda-Escudé et al. 1996; Hernquist, Katz & Weinberg 1996; Wadsley & Bond 1996; Zhang et al. 1997; Theuns et al. 1998; Machacek et al. 2000; see, for example, Efstathiou, Schaye & Theuns 2000, for a recent review).

In photoionization equilibrium, the optical depth, τ , is related to the overdensity of the gas, $\Delta \equiv \rho/\langle\rho\rangle$, by

$$\tau \propto \Delta^2 T^{-0.7} / \Gamma_{12} \propto \Delta^{2-0.7(\gamma-1)} / \Gamma_{12}. \quad (1)$$

[★]Based on observations collected at the European Southern Observatory, under the Large Programme ‘Cosmological Evolution of the Intergalactic Medium’ ID No. 166.A-0106 with the Ultraviolet and Visible Echelle Spectrograph on the 8.2-m Kueyen telescope operated at the Paranal Observatory, Chile.

[†]E-mail: rollinde@iap.fr

Here, $\Gamma = \Gamma_{12} 10^{-12} \text{ s}^{-1}$ is the hydrogen photoionization rate and $T(\Delta)$ is the temperature of the gas. The associated transmission $F = \exp(-\tau) \equiv F_o/F_c$ is the observed flux (F_o) divided by the estimated continuum flux (F_c). Photoionization heating and cooling by adiabatic expansion introduce a tight relation $T = T_0 \Delta^{\gamma-1}$ in the low-density IGM responsible for the Lyman α forest (Hui & Gnedin 1997; Theuns et al. 1998). The above equation has been extensively used, especially to probe the matter clustering (Hui 1999; Nusser & Haehnelt 1999; Pichon et al. 2001; Viel et al. 2002b; Croft et al. 2002; McDonald 2003; Rollinde et al. 2003).

The UV-background that causes the photoionization is dominated by massive stars and quasars (Giroux & Shapiro 1996; Haardt & Madau 1996). The amplitude of the corresponding photoionization rate as a function of redshift, $\Gamma(z)$, and the relative importance of the different sources, are relatively uncertain. Fardal, Giroux & Shull (1998) have derived the H I and He II photoionization history by modelling the opacity of the IGM, using high-resolution observations of H I absorption. They find $\Gamma_{12} = 1-3$ at redshift $z = 2-4$. Haardt & Madau (2001) have combined models for the emissivity of galaxies and quasars with calculations of the absorption of UV photons in the IGM, and estimate $\Gamma_{12} \approx 1-2$ at redshift $z = 2-3$. More recent observations suggest that Lyman break galaxies may dominate the UV-background at $z = 3$ (Steidel, Pettini & Adelberger 2001). In simulations, assuming a standard big bang baryon fraction, the value of Γ_{12} has to be between 0.3 and 2 at a redshift $z = 2-3$ in order to reproduce observed Lyman α forest properties, such as the mean transmission and the column density distribution (Hernquist et al. 1996; Miralda-Escudé et al. 1996; Rauch et al. 1997; Zhang et al. 1997; Choudhury et al. 2001a; Haehnelt et al. 2001; McDonald & Miralda-Escudé 2001, 2003; Hui et al. 2002; Tytler et al. 2004; Bolton et al. 2005).

An independent way to estimate Γ is the proximity effect. Locally, the UV-field may be dominated by a single source, such as a bright quasar, leading to a deficit of absorption lines sufficiently close to the quasar. Because the amount of absorption is, in general, increasing with redshift, this reversal of the trend for redshifts close to the emission redshift of the quasar is called the ‘inverse’ or ‘proximity’ effect (Carswell et al. 1982; Murdoch et al. 1986). The strength of this effect depends on the ratio of ionization rates from quasar and UV-background, and because the quasar’s ionization rate can be determined directly, Γ_{12} can be inferred. This method was pioneered by Bajtlik, Duncan & Ostriker (1988) but more recent data have yielded a wide variety of estimates (Lu, Wolfe & Turnshek 1991; Kulkarni & Fall 1993; Bechtold 1994; Cristiani et al. 1995; Fernandez-Soto et al. 1995; Giallongo et al. 1996; Lu et al. 1996; Srianand & Khare 1996; Cooke, Espey & Carswell 1997; Scott et al. 2000, 2002; Liske & Williger 2001). Scott et al. (2000) collected estimates from the literature which vary over almost an order of magnitude at $z = 3$, i.e. $1.5 \lesssim \Gamma_{12} \lesssim 9$.

In the standard analysis of the proximity effect it is assumed that the matter distribution is not altered by the presence of the quasar. The only difference between the gas close to the quasar and far away is the increased photoionization rate in the vicinity of the quasi-stellar objects (QSOs). An important consequence is that the strength of the proximity effect should correlate with the luminosity of the quasar but such a correlation has not been convincingly established (see Lu et al. 1991; Bechtold 1994; Srianand & Khare 1996; see however Liske & Williger 2001). It is in fact likely that the quasar will be in an overdense region. Indeed, the presence of Lyman α absorption lines with redshift z_{abs} greater than the quasar redshift z_{em} suggests possible excess clustering of the IGM material

around QSOs (Loeb & Eisenstein 1995; Srianand & Khare 1996). Furthermore, in hierarchical models of galaxy formation, the super-massive black holes that are thought to power quasars are in massive haloes (Magorrian et al. 1998; Marconi & Hunt 2003; Häring & Rix 2004), which are strongly biased to high-density regions. If the accretion rate in quasars is close to the Eddington limit, then it seems plausible that the IGM density close to the quasar is significantly higher than the mean.

Recent studies of the transverse proximity effect by Croft (2004) and Schirber, Miralda-Escudé & McDonald (2004) also suggest excess absorption over that predicted by models which assume the standard proximity effect and isotropic quasar emission. If this is not due to an increase in density close to the quasar, it might imply that the quasar light is strongly beamed, or alternatively that the quasar is highly variable. Interestingly, neither of these affects the longitudinal proximity effect discussed in this paper.

Observations of the IGM transmission close to Lyman break galaxies (LBGs) show that the IGM contains more neutral hydrogen than the global average at comoving scales $1 < r \text{ (Mpc)} < 5 h^{-1}$ (Adelberger et al. 2003). As the UV photons from the LBGs cannot alter the ionization state of the gas at such large distances, it is most likely that the excess absorption is caused by the enhanced IGM density around LBGs. It is worth noting that various hydrodynamical simulations have trouble reproducing this so-called galaxy proximity effect (e.g. Bruscoli et al. 2003; Kollmeier et al. 2003; Maselli et al. 2004; Desjacques et al. 2004). If a similar excess of density around quasar host galaxies exists and is not taken into account, then a determination of Γ from the proximity effect will be biased high.

In this paper, we present a new analysis of the proximity effect of very bright quasars observed as part of the European Southern Observatory–Very Large Telescope (ESO–VLT) Large Programme (LP) ‘Cosmological Evolution of the Intergalactic Medium’ (PI Jacqueline Bergeron). This new method allows one to infer the density structure around quasars. The method is based on the cumulative distribution function (CDF) of pixel optical depth, τ , and so avoids the Voigt profile fitting and line counting traditionally used. Using τ instead of the transmission, $F = \exp(-\tau)$, has the great advantage that we can take into account the strong redshift dependence $\langle \tau \rangle \propto (1+z)^\alpha$, with $\alpha \approx 4.5$.

We begin by briefly describing the data used in this paper. We outline the procedure in Section 3 and illustrate it using hydrodynamical simulations in Section 4. The application to the high signal-to-noise and high-resolution spectra of the ESO–VLT LP is described in Section 5. Our analysis requires that the density be higher close to the quasar. Results and future prospects are discussed in Section 6. Throughout this paper, we assume a flat Universe with $\Omega_m = 0.3$, $\Omega_\Lambda = 0.7$ and $h = 0.7$.

2 THE DATA

2.1 Large Programme quasar sample

The observational data used in our analysis were obtained with the Ultraviolet and Visible Echelle Spectrograph (UVES) mounted on the ESO Kueyen 8.2-m telescope at the Paranal observatory for the ESO–VLT LP ‘Cosmological Evolution of the Intergalactic Medium’ (PI Jacqueline Bergeron). This programme has been devised to gather a homogeneous sample of echelle spectra of 18 QSOs, with uniform spectral coverage, resolution and

Table 1. Properties of the LP QSOs in our sample. The redshift of emission (details are given in columns 2–4) has been determined using different emission lines. The luminosity, L , in $h^{-2} \text{ erg s}^{-1} \text{ Hz}^{-1}$ (last column) is computed assuming an $\Omega_m = 0.3$ flat Universe and a spectral index of 0.5. Average determinations of z_{em} are taken from (2) Espey et al. (1989), (3) Bechtold et al. (2002) and Srianand & Khare (1996), using a correction factor suggested by (4) Fan & Tytler (1994) and Tytler & Fan (1992), or (re)done in this paper (1, Section 2.1).

Quasar	Mean value	z_{em} Used lines	Ref.	$\log(L)$
Q0122–380	2.203	H α , Mg II	2	31.633
PKS1448–232	2.220	H α , Mg II	2	31.527
PKS0237–23	2.233	H α , Mg II	2	31.665
HE0001–2340	2.267	Mg II	1	31.649
Q0109–3518	2.404	Mg II	1	31.819
HE2217–2818	2.414	Mg II	1	31.994
Q0329–385	2.440	H α , Mg II	2	31.278
Q0453–423	2.658	Lyman α , C IV, Si IV	3	31.709
PKS0329–255	2.736	C IV	1	31.577
Q0002–422	2.767	Lyman α , C IV, Si IV	3	31.721
HE0940–1050	3.068	C IV	1	32.146
PKS2126–158	3.267	Lyman α , C IV, Si IV	4	32.132

signal-to-noise ratio suitable for studying the IGM in the redshift range 1.7–4.5. Spectra were obtained in service mode observations spread over four periods (two years) covering 30 nights under good seeing conditions (≤ 0.8 arcsec). The spectra have a signal-to-noise ratio of $\sim 40\text{--}80 \text{ pixel}^{-1}$ and a spectral resolution $\geq 45\,000$ in the Lyman α forest region. Details of the data reduction can be found in Chand et al. (2004) and Aracil et al. (2004). In our analysis we have only used absorption lines that are between the Lyman α and the Lyman β emission lines of the quasar.

Six of the 18 LP QSOs (HE 1158–1843, HE 1347–2457, HE 0151–4326, HE 1341–1020, Q 0420–388 and HE 2347–4342) show signatures of associated absorption close to the emission redshift of the QSO, and are therefore excluded from our analysis. The remaining 12 are listed in Table 1, which gives the name of the QSO, its redshift, z_{em} , and the monochromatic luminosity at the Lyman limit (L).

An accurate determination of the emission redshift is important for the analysis. Espey et al. (1989) have found that the H α line is redshifted by an average 1000 km s^{-1} with respect to lines from high ionization species and has statistically a similar redshift as the lines from the low-ionization species. The mean difference between H α and Mg II redshifts in their sample is $\sim 107 \text{ km s}^{-1}$ with a standard deviation of $\sim 500 \text{ km s}^{-1}$. A redshift measurement based on H α and other low ionization lines is available for four of the QSOs (Espey et al. 1989; see Table 1). We consider the mean redshift of all observed lines for these systems. When the Mg II emission line is observed, as it is for three additional QSOs, we fit the profile with the doublet of Mg II and a polynomial continuum to determine accurately the redshift. Fig. 1 shows the results of this fitting procedure for the three QSOs. On average, these redshifts should be within an rms of 500 km s^{-1} from the systemic redshift. For two of the QSOs, Bechtold et al. (2002) and Srianand & Khare (1996) used the C IV, Si IV and Lyman α lines to determine the redshift of emission, and applied the correction factor suggested by Fan & Tytler (1994). Otherwise, we use the C IV emission line for two other QSOs and the determination from Tytler & Fan (1992) for the last remaining QSO. Therefore, seven out of 12 redshifts of the QSOs in our sample are determined accurately using the H α or Mg II emis-

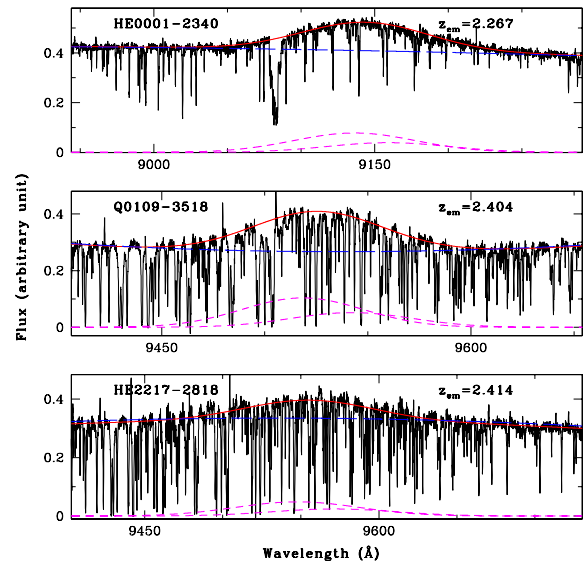


Figure 1. Determination of the emission redshift, z_{em} , of three QSOs using the Mg II line (see Table 1). For each quasar, the Mg II emission lines ($\lambda\lambda$ 2796.35, 2803.53) are fitted (two dashed lines) on the top of a polynomial continuum (long-dashed line). The final profile is shown with a solid line.

sion line, and two using the correction factor from Fan & Tytler (1994).

The QSO luminosity at the Lyman limit is computed from the available B magnitude. The QSO continuum slope is assumed to be a power law, $F_\lambda \sim \lambda^\alpha$. We use $\alpha = -0.5$ as Francis (1993). We checked that within a reasonable range of $\alpha = -0.5$ to -0.7 (e.g. Cristiani & Vio 1990), our main result (i.e. the density structure around quasar) is not affected by our choice of α .

All possible metal lines and Lyman α absorption of a few sub-DLA systems (there are no DLA systems in the observed spectra) are flagged inside the Lyman α forest. The entire line is removed up to the point where it reaches the continuum. We have not removed the Lyman α absorption associated with metal line systems (i.e. systems with $N(\text{H I}) < 10^{19} \text{ cm}^{-2}$) but the metal absorption lines themselves are flagged and removed.

Continuum fitting of the quasar spectra is very important for our analysis. As most of the QSOs in our sample are at lower redshifts where line-crowding is not a problem, all the available line-free regions are used to fit the continuum. The procedure used to compute the continuum has been calibrated and controlled using synthetic spectra by Aracil et al. (2004). They estimated that errors in the continuum amount to about 2 per cent at $z \sim 2.3$. The transmission $F = \exp(-\tau)$ for each quasar in Table 1 is shown in Fig. 2 up to a luminosity distance of $20 h^{-1} \text{ Mpc}$.

2.2 Mock Large Programme quasar sample

We use mock spectra generated from hydrodynamical simulations to illustrate and test the method described below. The simulated cosmological model has $(\Omega_m, \Omega_\Lambda, h, \Omega_b h^2, \sigma_8) = (0.3, 0.7, 0.65, 0.019, 0.9)$, where the symbols have their usual meaning, and we have used CMBFAST (Seljak & Zaldarriaga 1996) to generate the linear power spectrum at the starting redshift $z = 49$, assuming scale-invariant $n = 1$ primordial Gaussian fluctuations. The baryons are heated and ionized by an imposed uniform ionizing background as computed by Haardt & Madau (1996), and updated by Haardt &

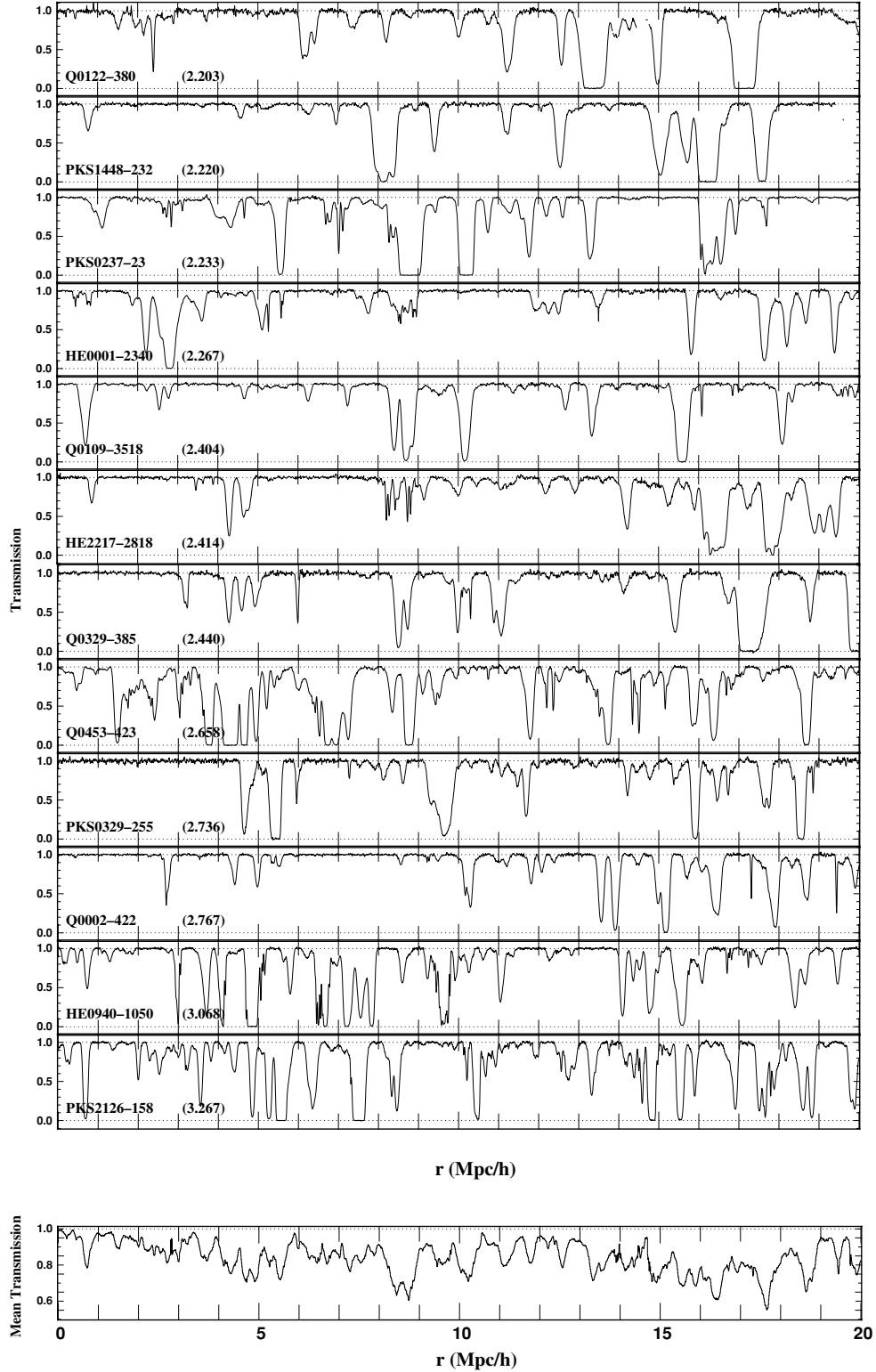


Figure 2. Transmission $F = \exp(-\tau)$ as a function of luminosity distance for the LP QSOs listed in Table 1. The emission redshift, z_{em} , is indicated between brackets and increases from top to bottom. The evolution of the optical depth with redshift (see Section 3.4) is removed to compute the mean transmission $\bar{F} = \langle \exp[-\tau/\bar{\tau}(z)] \rangle$ as a function of luminosity distance (bottom panel). The proximity effect is clearly seen as an increase in mean transmission close to the quasar.

Madau (2001). We have increased the photoheating rates during hydrogen and helium reionization to satisfy the constraints on the temperature of the IGM as determined by Schaye et al. (2000). This ionizing background was referred to as ‘designer model’ in that

paper. In this model, hydrogen reionizes at $z = 6.5$ and helium at $z = 3.5$. The amplitude of this background is scaled so that the mock spectra reproduce the evolution of the mean transmission $\exp(-\tau)$ with redshift. The simulation is performed with a modified version

of HYDRA (Couchman, Thomas & Pearce 1995) as described in more detail in Theuns et al. (1998). HYDRA combines smoothed particle hydrodynamics (SPH; Lucy 1977; Gingold & Monaghan 1977) to represent the gas, and P3M (Couchman 1991; Hockney & Eastwood 1981) to solve Newtonian gravity. It follows the evolution of a periodic, cubic region of the Universe of comoving size $20 h^{-1}$ Mpc to a redshift $z = 1.7$, using 256^3 particles of each species, and a comoving gravitational softening of $20 h^{-1}$ kpc. Non-equilibrium gas cooling and photoheating is implemented, using the rates of Theuns et al. (1998). Cold, dense gas particles are converted to collisionless stars, but there is no feedback included. The resolution of the simulations is close to sufficient to resolve the Lyman α forest.

As the simulation is running, we store the physical state of the IGM along many thousands of uncorrelated sight lines, which are later patched together into mock spectra with a large redshift extent. A full simulated spectrum typically requires around 20 individual sightlines through the simulation box, at $z = 2$. We use the photoionization package CLOUDY¹ to compute the ionization balance of the gas in the optically thin limit, in the presence of the Haardt & Madau (2001) ionizing background. We generate 20 mock spectra for each of our observed quasars taking into account the excess ionization by a QSO of luminosity similar to the mean luminosity of the QSOs in our sample. A mock spectrum for a given QSO extends over the same wavelength range as that QSO, has the same pixel size and spectral resolution, and we add noise to the simulated spectra with the same wavelength and flux dependence. Except for metals, which are flagged in the real data and are not used in this analysis, this procedure ensures that we impose the same biases in the reconstruction of the mock spectra, as are present in the real data. The analysis procedure described next does not rely on simulations; we only use simulated spectra to demonstrate that the method works.

3 METHOD

3.1 Overview

Our aim is to investigate the density structure around high-redshift luminous quasars. We do so by investigating how the probability distribution (PDF) of optical depths, $P(\tau)$, varies with distance to the quasar. Far away from the QSO, $P(\tau, z)$ evolves with redshift mainly because the mean optical depth decreases with redshift due to the expansion of the Universe. In Appendix A we show that the shape of the PDF does not evolve much over the relatively small redshift range $1.8 \leq z \leq 3.1$ covered by our QSO sample. Therefore, we can define a redshift-independent scaled optical depth distribution, $P(\tau, z) \equiv P[\tau(z)/\tau_0(z)]$, which allows us to predict the optical depth PDF at any z . The ability to take into account the strong redshift evolution of the mean optical depth is a major advantage of our method.

We can now compare this predicted optical depth PDF with the measured one, as a function of distance r to a QSO. We show that this predicted PDF differs significantly from the measured PDF close to the QSO. Indeed, radiation from the QSO will decrease the neutral hydrogen fraction in its surroundings, which in turn will lead to a decrease of the reference optical depth. This is the usual proximity effect. In contrast, if the QSO lives in a high-density environment, as is expected, then the optical depth will increase. Therefore, we need to introduce another function $f(r)$, which describes the effect of the QSO on the PDF, such that the optical depth scales as $\tau/[f(r)\tau_0(z)]$.

When radiation dominates, $f(r) \ll 1$, and the optical depth becomes very small. When density dominates, $f(r) \gg 1$, and the optical depth becomes very large. The explicit expression for $f(r)$ is given in equation (9). Of course, the presence of the QSO might also change the shape of the PDF. Our main assumption in this paper is that the shape does not change, and we demonstrate below that this is a good assumption.

By comparing the predicted to the measured optical depth PDFs, we can determine the relative importance of radiation versus density enhancement. As we explain in more detail below, we can offset a higher amplitude of the background ionization rate with a decrease in the overdensity; our determination is degenerate in this respect. So instead of assuming no overdensity and inferring the background ionization rate, $\Gamma(z)$, as is usually done in the analysis of the proximity effect, we will assume a given value of $\Gamma(z)$, and recover the corresponding overdensity.

This method is based on comparing optical depth PDFs. We characterize the difference between two PDFs, by computing the maximum absolute difference between the corresponding cumulative PDFs. Given bootstrap resampled realizations of these PDFs, we can associate a probability to a given difference in cumulative PDFs. This then allows us to associate a given probability of the overdensity as a function of distance to the QSO, for an assumed value of the ionization rate. This is the basis for the inferred overdensity as a function of distance to the LP QSOs shown in Fig. 10.

In the rest of this section we explain this procedure in more detail, and test it on our mock QSO spectra. Readers not interested in these details may want to skip directly to Section 5, where we apply the method to the LP data.

3.2 Optical depth–density relation

We analyse the proximity effect using the cumulative distribution of pixel optical depths as a function of distance to a quasar. The starting point is equation (1), which relates optical depth, τ , to overdensity, $\Delta = \rho/\langle\rho\rangle$,

$$\tau = \tau_0 \Delta^2 \propto \Delta^{1/(1+\beta)}, \quad (2)$$

where $1/(1+\beta) = 2 - 0.7(\gamma - 1)$, and

$$\tau_0 = 0.206 \left(\frac{\Omega_b h^2}{0.02} \right)^2 \frac{X}{0.24} \frac{X + 0.5Y}{0.88} \frac{\alpha(T)}{\alpha(T_4)} \times \frac{1}{\Gamma_{12}} \frac{H(z=2)}{H(z)} \left(\frac{1+z}{3} \right)^6, \quad (3)$$

is the Gunn–Peterson (Gunn & Peterson 1965) optical depth. Here, $\alpha(T_4 = 10^4 \text{ K}) = 4.19 \times 10^{-13} \text{ cm}^3 \text{ s}^{-1}$ is the hydrogen recombination coefficient (Verner & Ferland 1996), which scales approximately $\propto T^{-0.7}$ close to $T = 10^4 \text{ K}$, $H(z)$ is the Hubble constant at redshift z , X and Y are the hydrogen and helium abundances by mass, respectively, and $\Omega_b h^2$ is the baryon fraction. We have assumed that hydrogen and helium are both almost fully ionized. The exponent γ and normalization T_0 of the temperature–density relation $T = T_0 \Delta^{\gamma-1}$, have been measured by, for example, Schaye et al. (2000) to be in the range $\gamma = [1 - 1.5]$ and $T_0 \approx 10^4 \text{ K}$ in the redshift interval $2 \leq z \leq 3$. How are the density and optical depth PDFs related?

Let $P_\Delta(\Delta, z) d\Delta$ be the density distribution at redshift z . The PDF for the optical depth $P_\tau(\tau, z) d\tau$ is obtained by combining $P_\Delta(\Delta, z) d\Delta$ with equation (2). At two different redshifts z_1 and z_2 , say, $P_\tau(\tau, z) d\tau$ will differ because τ_0 changes (see equation 3) and because the density PDF, $P_\Delta(\Delta, z) d\Delta$, evolves as structure

¹ See <http://www.nublado.org/>.

grows. For the relatively small redshift range covered by the LP quasars, we show below that the redshift evolution of $P_\tau(\tau, z) d\tau$ is dominated by that of the mean optical depth, τ_0 , and that the shape of the distribution does not change very much. This is true for the simulated quasar sample as well. The PDF of τ is therefore given by

$$P_\tau(\tau, z) d\tau \approx (1 + \beta) P_\Delta \left[\left(\frac{\tau}{\tau_0} \right)^{1+\beta} \right] \left(\frac{\tau}{\tau_0} \right)^\beta \frac{d\tau}{\tau_0}, \quad (4)$$

and to a very good approximation, its redshift dependence is through $\tau_0(z)$ only. Therefore, given the PDF of τ at several redshifts covered by the LP sample, $1.7 \leq z \leq 3.1$, one can accurately predict the scaling factor required to scale each PDF $P_\tau(\tau, z)$ to the PDF observed at a given reference redshift, $z = 2.25$. We will call this the ‘scaled optical depth PDF’ below. We emphasize here that the transmission is non-linearly related to the density. Because the median optical depth corresponds to a value of the flux within the noise around the continuum, the evolution with redshift cannot be taken into account with the transmission only.

Thermal broadening and peculiar velocities prevent the unique identification of an overdensity, Δ , in real space, with a given optical depth, τ , in redshift space. Therefore, $P_\Delta(\Delta, z) d\Delta$ does not refer to the real space overdensity, but the optical depth weighted overdensity, as used for example in Schaye et al. (1999). In Appendix A we discuss a fitting function of P_Δ which is based on the fit introduced by Miralda-Escudé, Haehnelt & Rees (2000) for the density distribution of the IGM. We show there that the shape of this function fits P_Δ well, but the best-fitting parameters differ considerably from the real space density PDF. We also show that, in simulations, P_Δ varies little with redshift in $1.7 \leq z \leq 3.1$.

A quasar’s proximity effect will change the PDF of τ . The change due to the increase in ionization rate can be accurately predicted by the appropriate scaling of τ_0 . However, the density PDF may change, as is expected for biased quasar formation, which will modify accordingly the optical depth PDF. In our model, the shape of the density PDF is assumed to be unaltered, only the mean value is changed. This is our main assumption. Physically, this implies that feedback effects from the galaxy hosting the QSO, such as winds, infall, or excess of clustering that may modify the density distribution itself, are neglected. The net effect of the quasar is then a rescaling of τ_0 . This scaling factor is determined as a function of distance r to the quasar, by comparing the measured PDF of τ at r with that predicted at the same redshift. The method is based on τ , whereas what we observe is the transmission $F = \exp(-\tau)$. We describe how to infer τ from F next.

3.3 Optical depth distribution

At a given redshift only part of the PDF of optical depth, $P_\tau(\tau) d\tau$, can be recovered from the observational data. Low values of τ , $\tau \leq \tau_{\min}$, are lost in the noise, whereas high values of τ , $\tau \geq \tau_{\max}$, cannot be recovered because the Lyman α absorption is saturated. However, we can estimate the range $\tau_{\min} \leq \tau \leq \tau_{\max}$ where τ can be accurately recovered given the noise properties of the data.

By using higher-order transitions, one can accurately recover high values of τ where Lyman α is saturated but Lyman β , for example, is not (Savage & Sembach 1991; Cowie & Songaila 1998; Rollinde, Petitjean & Pichon 2001; Aguirre, Schaye & Theuns 2002; Aracil et al. 2004). However, here we only use the Lyman α absorption from normalized spectra and recover τ between $\tau_{\min} = -\log(1 - 3\sigma) \simeq 0.1$ and $\tau_{\max} = -\log(3\sigma) \simeq 2.5$, where $\sigma(\lambda)$ is the rms noise

as a function of wavelength. Note that $\tau_{\min} = 0.1$ is a high value compared to the actual noise in most of the spectra. We use this limit to be conservative. Because we will use the cumulative probability distribution of τ (CPDF; in the following all probability functions implicitly refer to P_τ , unless explicitly noted), we also keep track of the number of pixels below τ_{\min} and above τ_{\max} . The CPDF of this censored representation of the optical depth, $\text{CPDF}_{\text{rec}}(\tau)$, is therefore a portion of the full CPDF, $\text{CPDF}(\tau) \equiv P(\tau' < \tau)$, between τ_{\min} and τ_{\max} :

$$\begin{aligned} \text{CPDF}_{\text{rec}}(\tau) &= 0 & \tau < \tau_{\min} \\ \text{CPDF}_{\text{rec}}(\tau) &= \text{CPDF}(\tau) & \tau_{\min} \leq \tau \leq \tau_{\max} \\ \text{CPDF}_{\text{rec}}(\tau) &= 1 & \tau > \tau_{\max}. \end{aligned} \quad (5)$$

The values of τ_{\min} and τ_{\max} depend on redshift because the noise level σ does, but this dependence is very weak for our sample. This means that when we scale two recovered PDFs to the same reference redshift, the scaled values of τ_{\min} and τ_{\max} will no longer be the same. For example, at lower redshift (say, $z = 2$) higher overdensities $\Delta \propto [\tau/\tau_0(z = 2)]^{1+\beta}$ can be recovered before the line becomes saturated compared with higher redshift ($z = 3$, say) because of the evolution of $\tau_0(z)$. Conversely, lower overdensities can be recovered at $z = 3$ than at $z = 2$, before the line disappears in the noise. This could be exploited to increase the effective recovered overdensity range if the evolution of τ_0 was strong enough. We describe how we scale PDFs to a common redshift next.

3.4 Scaling of the reference optical depth $\tau_0(z)$

We show in Sections 4.3 and 5 that the shape of the censored optical depth cumulative distribution function in both simulations and observations, is nearly independent of redshift. These distributions refer to regions far away from the quasar (proper distance $\geq 50 h^{-1}$ Mpc) where the distribution of τ is not modified by radiation from the QSO itself. The fact that the shape of the PDF is conserved means that redshift evolution can be modelled accurately by a simple redshift dependence of the reference optical depth, $\tau_0(z)$. We find the best-fitting scaling $\tau_0(z) \propto (1 + z)^\alpha$ by minimizing the maximum absolute distance between scaled optical depth CPDFs (KS distance) within different bins in redshift. Note that the evolution of the number of systems within a range of column densities, as used in most previous work on the proximity effect, is also described as a simple scaling. Errors in $\tau_0(z)$ are estimated using a bootstrap resampling of chunks of proper size $10 h^{-1}$ Mpc. In the next steps, $\tau_0(z)$ is used to scale the optical depth of each pixel to a reference redshift of $z = 2.25$.

3.5 Proximity effect

We now consider the influence of a quasar on the optical depth distribution in the nearby IGM, scaled to the same reference redshift using the function $\tau_0(z)$. We consider the effect of both the ionizing flux emitted by the quasar and that of a modified density distribution.

Let the quasar emit ionizing photons with spectrum characterized in the usual way as

$$\begin{aligned} 4\pi J_L(\nu, r) &= \frac{L}{4\pi r^2} \left(\frac{\nu}{\nu_{\text{HI}}} \right)^{-\phi} \text{erg s}^{-1} \text{cm}^{-2} \text{Hz}^{-1} \\ &= 4\pi J_{21}(z) \times 10^{-21} \left(\frac{\nu}{\nu_{\text{HI}}} \right)^{-\phi} \omega(r, z). \end{aligned} \quad (6)$$

Here, L is the monochromatic luminosity of the quasar at the hydrogen ionization threshold ν_{HI} . The corresponding ionization rate

is $[12.6/(3 + \phi)] J_{21} \omega(r) 10^{-12} \text{ s}^{-1}$, when one approximates the hydrogen photoionization cross-section with a power law (Theuns et al. 1998, table B4). The function ω is

$$\omega(r, z) = \frac{L(h^{-2} \text{ erg s}^{-1} \text{ Hz}^{-1})/4\pi}{4\pi [r(z)(h^{-1} \text{ cm})]^2 10^{-21} J_{21}(z)} \equiv \left[\frac{r_L(z)}{r(z)} \right]^2. \quad (7)$$

Here $r(z)$ is the luminosity distance from the quasar at redshift z_{em} to the cloud at redshift z , at the time the photons arrive there. For a given pixel, r is computed from the absorption wavelength of that pixel and the emission redshift of the quasar, using the equations from Phillipps, Horleston & White (2002) for an $\Omega_m = 0.3$ flat cosmological model. [In the future, it would be worthwhile to investigate how our results depend on the assumed cosmology, as initiated for the standard proximity effect analysis by Phillipps et al. (2002).] Note that this neglects possible infall or outflow close to the quasar. All distances are computed as a luminosity distance in the analysis. Yet, we may also define them as proper distance because proper and luminosity distances are almost equal up to $30 h^{-1} \text{ Mpc}$ at the redshifts of interest here. All quasars in our sample have a similar luminosity (Table 1); they will then have a similar value of r_L when Γ_{12} does not vary strongly, as is expected (e.g. Haardt & Madau 1996; Fardal et al. 1998).

The total ionization rate Γ in the IGM is the sum of that from the uniform background radiation, $\Gamma^{\text{IGM}}(z)$, and from the radiation from the quasar, $\Gamma^Q(r, z)$. The increase in Γ will shift the PDF of τ to smaller values, without changing its shape. Very close to the QSO, $\Gamma(r) \propto 1/r^2$ diverges; hence, according to equation (3), $\tau_0 \rightarrow 0$, which is the usual proximity effect.

However, we argued before that the quasar is likely to be in an overdense region, which will lead to an increase in τ . We model this by assuming that the density close to the quasar is simply a scaled-up version of that far away from the quasar, i.e.

$$P_{\Delta}[r, [1 + \Psi(r)]\Delta] d\Delta \equiv P_{\Delta}(\Delta) d\Delta. \quad (8)$$

Equation (2) shows that this has the effect of increasing τ_0 by a factor $[1 + \Psi(r)]^{1/(1+\beta)}$, shifting the PDF of τ at a given r bin, to higher values without changing its shape. To simplify the notation, we will use $\rho/\langle\rho\rangle$ to refer to the density structure, or enhancement, around the quasar (i.e. $1 + \Psi$), and Δ to refer to the distribution of density P_{Δ} .

Note that we neglect a possible variation of temperature due to the ionizing flux from the quasar. Because the main modification to the ionizing background is the larger proportion of hard photons from the quasar, we assume that the change in temperature is not large enough to modify the optical depth distribution in a significant way. This argument will not be valid if He II is not ionized. Available observations indicate the epoch of He II reionization may be probably earlier than $z \simeq 3$ (e.g. Theuns et al. 2002).

The combined effect of a density increase and extra ionizing photons is to shift τ_0 by a factor

$$\tau_0 \rightarrow \tau_0 \frac{[\rho(r)/\langle\rho\rangle]^{1/(1+\beta)}}{1 + (r_L/r)^2}. \quad (9)$$

The relative importance of quasar versus UV-background ionizing photons is characterized by $r_L(z)^2 \propto L/\Gamma_{12}(z)$ (where $\Gamma^{\text{IGM}} = \Gamma_{12} 10^{-12} \text{ s}^{-1}$). In the absence of any temperature enhancement the optical depth at r is globally scaled compared to the optical depth in the IGM. As a consequence, the distribution $P(\tau)$ is simply scaled

along the abscissa toward higher values in the case of an overdensity ($\rho/\langle\rho\rangle > 1$) or lower values under the influence of the quasar ionizing flux ($\omega > 0$). Thus, for a given distance r , there is an intrinsic degeneracy between the local density structure $\rho(r)$ and the value of Γ_{12} , combined in the above scaling factor. Therefore, if one modifies the value of Γ_{12} , the recovered value of $[\rho(r)/\langle\rho\rangle]^{1/(1+\beta)}$, is scaled by a constant value $1/\Gamma_{12}$ when $r \ll r_L$ and is independent of Γ_{12} when $r \gg r_L$.

Close to or far away from the quasar, this scaling is constant, which allows the shape of the density enhancement to be recovered. Then, despite the fact that the absolute value of $\rho(r)$, when $r \ll r_L$, will depend on the value of Γ_{12} assumed in the analysis, the presence of a non-uniform density enhancement can in principle be revealed by this method. Conversely, if the underlying density enhancement is known through numerical simulations, for example, or if it is neglected as in the standard proximity effect analysis, Γ_{12} can be recovered. However, neglecting overdensities always implies an overestimate of Γ_{12} , irrespective of the method.

We now describe how the density structure is recovered and how errors are estimated.

3.6 Estimation of the density structure and errors

The density structure, $\rho(r)/\langle\rho\rangle$, can be inferred once the ionizing rate, $\Gamma_{12}(z)$, and the slope of the temperature–density relation, γ , are determined. We will illustrate how $\rho/\langle\rho\rangle$ changes with changes in these parameters.

The mean scaled CPDF in the IGM, and its statistical uncertainty, are determined from bootstrap resampling pixels outside the possible proximity region, at distances larger than $50 h^{-1} \text{ Mpc}$ proper. We characterize the difference between two PDFs by the maximum absolute distance (KS distance) between the corresponding cumulative distributions, just as in a Kolmogorov–Smirnov test. Bootstrap resampling allows us to associate a probability to a given value of this KS distance, $\mathcal{P}(\text{KS})$.

The proximity region is characterized by evaluating the scaled CPDF in radial bins from the background QSO. For each radial bin, the mean CPDF in the IGM is shifted according to equation (9), using our assumed value of Γ_{12} and for different values of the function $[\rho(r)/\langle\rho\rangle]^{1/(1+\beta)}$. Given the probability associated with a given value of KS, we can determine a probability associated with a given value of $\rho(r)$, $P_{\text{KS}}[\rho(r)/\langle\rho\rangle]$. The distribution of KS values of course depends on the number of pixels in each bin. Because we want to use small bins close to the QSO, we need to determine the probability $\mathcal{P}(\text{KS})$ for each bin separately, using only pixels outside the proximity region.

We bootstrap the QSO sample, using different subsamples of six quasars taken from the 12 quasars available in the full sample. We can then define a global probability associated with $\rho(r)$ as

$$P[\rho(r)/\langle\rho\rangle] \equiv \langle P_{\text{KS}}[\rho(r)/\langle\rho\rangle] \rangle_{\text{subsample}}, \quad (10)$$

which will allow us to characterize the density structure at different level of confidence.

Note that this method is also able to recover Γ_{12} , if one assumes $\rho(r) \equiv \langle\rho\rangle$, i.e. the assumption made in the standard analysis of the proximity effect. Indeed, the above procedure can be done for different values of Γ_{12} , while maximizing the product of $P[\rho(r) \equiv \langle\rho\rangle]$ over r .

We will first apply the method to mock spectra in order to show that this method works well. We also use the simulations to show that our method of bootstrap sampling chunks and quasars gives realistic errors.

4 PROXIMITY EFFECT USING OPTICAL DEPTH: VALIDATION OF THE METHOD WITH SYNTHETIC SPECTRA

In this section, we use mock LP spectra, generated as described in Section 2.2. The proximity effect is implemented as described by equation (9), assuming the mean luminosity of the LP sample, $L = 5.4 \times 10^{31} h^{-2} \text{ erg s}^{-1} \text{ Hz}^{-1}$ and $\Gamma_{12} = 1$, without and with additional density enhancement. Note that the value used for Γ_{12} here need not be equal to the value actually implemented in the simulation itself. The different steps involved in the analysis, as described above, are now applied successively to the mock spectra. Our assumptions and the ability of the method to recover the density structure will be discussed.

4.1 Evolution of the optical depth with redshift

As we are first interested in the evolution of the optical depth in the IGM, we consider here pixels at a distance larger than $50 h^{-1}$ Mpc proper to the quasar only. The evolution of the CPDF within five bins in redshift centred at $z = 1.8, 2.0, 2.25, 2.5$ and 2.95 is displayed in the top panel of Fig. 3. The main evolution is driven by the mean density that increases, together with the mean optical depth $\tau_0(z)$, with redshift. This corresponds to a shift of the CPDF along the abscissa toward higher values. As explained in Section 3.4, a simple scaling of the reference optical depth $\tau_0(z)$ is used to remove this primary evolution. Parametrizing $\tau_0(z) \propto (1+z)^\alpha$ gives a best-fitting value of $\alpha \approx 4.5$. Although some scatter is present, half of 50 different samples prefer a value $4 \leq \alpha \leq 4.5$. Once the optical depth at each pixel is scaled using this relation, the CPDF computed within the same bins is displayed in the bottom panel of Fig. 3. We find then that the shape is indeed conserved, to the level of accuracy of our sample. In our mock samples, the ionizing background $\Gamma(z)$ varies only weakly with z over the range $1.7 \leq z \leq 3.1$, as does the temperature T of the IGM. Therefore, a scaling close to $\alpha = 4.5$ is indeed expected from equation (3), given the high-redshift approximation $H(z) \propto (1+z)^{3/2}$. Below we will generate several observed data sets by bootstrapping the LP quasars, and use either the best-fitting exponent in $\tau_0(z) \propto (1+z)^\alpha$ for each sample, or a fixed value of $\alpha = 4.5$.

4.2 Proximity effect

Once the main evolution of optical depth with redshift is removed, we can concentrate on its change with distance to the quasar. Fig. 4 shows the evolution of different percentiles of the optical depth with luminosity distance to the mock background quasar. Note that we only model the excess ionizing radiation from the QSO; there is no overdensity at the emission redshift (i.e. $\rho/\langle\rho\rangle = 1$). We note that the relation between ω and distance (equation 7) depends on the luminosity of the quasar. In our homogeneous sample, the luminosity of the QSOs, and then ω , varies only within a factor of 2 from one quasar to another. For the mock spectra, because we assume a unique value of the luminosity of each quasar, the distance at which $\omega = 1$ is the same for all mock spectra; it is shown as a vertical line in the figure. The effect of assuming a different luminosity on the recovered overdensity is discussed in more detail in Section 5.

Fig. 4 clearly reveals the decrease of τ with decreasing radius, as the mock QSO starts dominating the ionization rate. Because in this case $\rho/\langle\rho\rangle = 1$, the optical depth where $\omega = 1$ must be a factor of 2 less than its value in the ambient IGM at $r > 50 h^{-1}$ Mpc (equation 9). This is indeed observed here, for each percentile. Note how

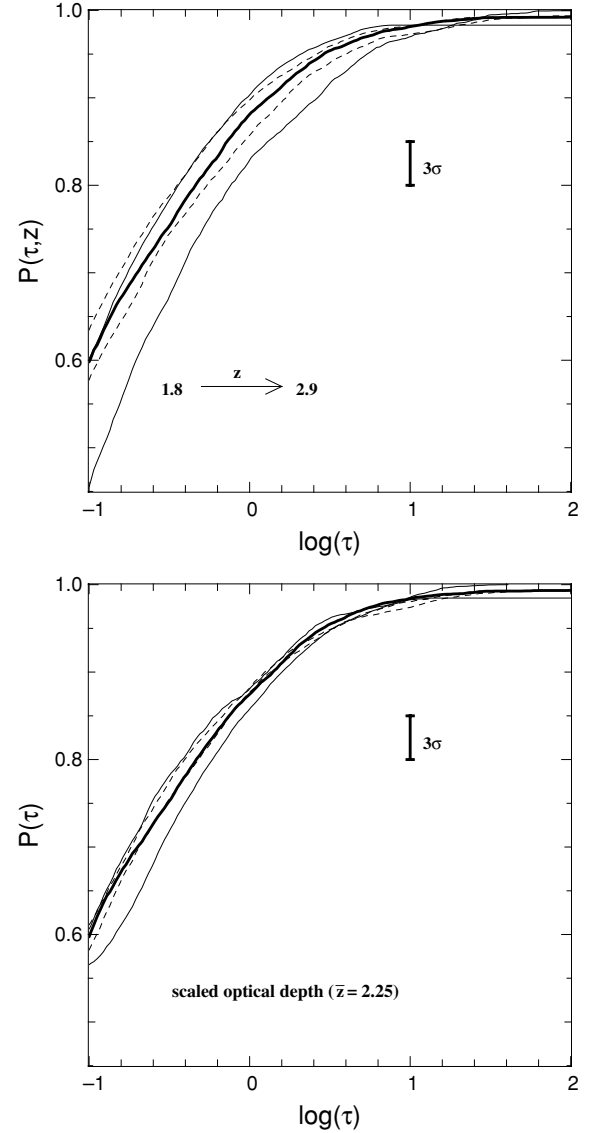


Figure 3. Evolution with redshift of the cumulative distribution of optical depth, computed with mock LP spectra. Only pixels located far away from the proximity region are considered. Top panel: cumulative distributions in five bins in redshifts centred on $z = 1.8, 2.0, 2.25, 2.5$ and 2.95 (left to right, with alternate solid and dashed lines). The 3σ statistical error is shown with a vertical mark in both panels. Bottom panel: same distributions but after scaling each curve to the CPDF at $z = 2.25$ (thick curve in both panels) by a redshift-dependent scaling factor $\tau \rightarrow \tau \tau_0(z = 2.25)/\tau_0(z)$. The scaled curves are all consistent within the 3σ error, showing that the shape of the distribution is independent of z .

at small distances the optical depth is everywhere decreased below τ_{\min} , and how the different percentiles are almost all equal to the minimum optical depth.

4.3 Recovery of a uniform density field

This qualitative change with distance is now studied quantitatively to recover the underlying density field close to the background quasars. During the implementation of the proximity effect in the mock spectra, we assumed $\Gamma_{12} = 1$. Therefore, we shall use the same value in the analysis. A wrong estimate of Γ_{12} mostly leads to a rescaling

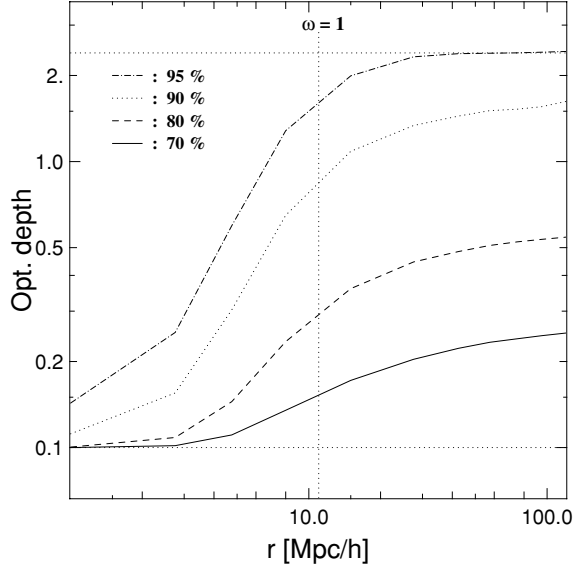


Figure 4. Evolution of different percentiles of the scaled optical depth ($z = 2.25$) with luminosity distance to the background quasar, in mock LP spectra. Quasars are randomly located in the simulation box, which implies that no additional density structure around the quasars is expected statistically (i.e. $\rho/\langle\rho\rangle = 1$). Mock spectra are computed assuming the mean luminosity of the LP sample, $L = 5.4 \times 10^{31} \text{ h}^{-2} \text{ erg s}^{-1} \text{ Hz}^{-1}$ and $\Gamma_{12} = 1$. The distance where the amplitude of the ionizing flux from the quasar and in the IGM are equal (i.e. $\omega = 1$, equation 7) is indicated by the vertical dashed line. Horizontal lines indicate the observational upper and lower limits in optical depth.

of $\rho/\langle\rho\rangle$ in the region of interest, close to the quasar. Although the simulation does not correspond to a unique value of γ (there is a dispersion in the temperature–density relation), the exact assumed value, if within the range specified above (equation 2), does not have a large influence on the recovered density; we assume here $\gamma = 1.5$. We will illustrate the amplitude of these effects on the analysis of the LP quasars in Section 5. Here, because the quasars are randomly distributed in the simulation box, we must recover a uniform density with $\rho(r) = \langle\rho\rangle$.

For each bootstrap sample (Section 3.6), we recover a different function $\tau_0(z)$ for the evolution of τ . However, very similar results are obtained using a fixed evolution $(1+z)^{4.5}$, which shows that errors on the estimation of $\tau_0(z)$ are not essential in the analysis. We then fit the change of the CPDF with distance to the quasar (Fig. 4) using equation (9). This allows us to recover a probability distribution of $\rho(r)/\langle\rho\rangle$, from the function P_{KS} (equation 10).

Our result is therefore expressed in terms of a probability for each value of $\rho/\langle\rho\rangle$ at a given radius. Different levels of probability are shown in Fig. 5. The 2σ and 3σ levels of confidence correspond to the grey region and to the solid lines, respectively. The input structure $\rho/\langle\rho\rangle = 1$ is indeed accurately recovered at the 2σ level for $r > 1 \text{ h}^{-1} \text{ Mpc}$. In this particular case, the assumption of the standard proximity effect is satisfied (see Section 1). Then, assuming $\rho/\langle\rho\rangle \equiv 1$, the data (i.e. the optical depth CPDF in our analysis, but also the mean flux²) are fitted with $\Gamma = \Gamma_{\text{true}}$ within the 3σ confidence level.

² If the distribution of τ is known between τ_{min} and τ_{max} , then the distribution of the flux is known between 0 and 1, which allows us to compute the mean flux too.

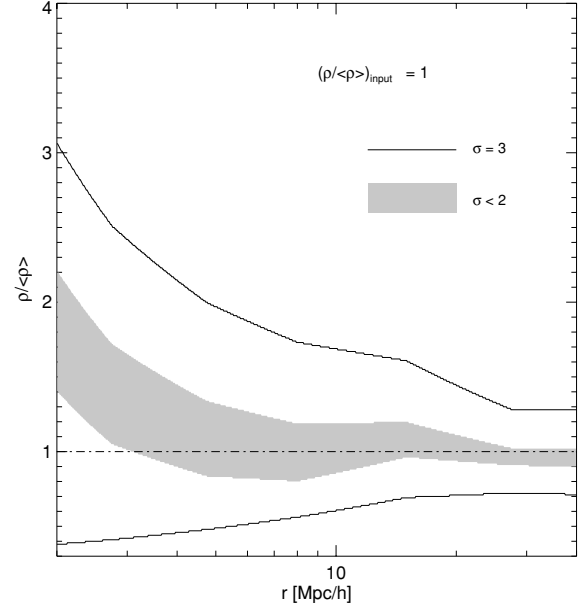


Figure 5. Recovered density structure versus luminosity distance to the background quasar, from the analysis of mock LP spectra. Mock spectra, including additional ionization from the background quasar, are generated from randomly positioned quasar (i.e. $\rho_{\text{input}}/\langle\rho\rangle = 1$). The 2σ and 3σ confidence levels are indicated as grey region and solid lines, respectively. The input structure is well within the 2σ confidence level except for a small bias, and a large increase of errors below $\approx 10 \text{ h}^{-1} \text{ Mpc}$ proper (luminosity and proper distances are similar up to $30 \text{ h}^{-1} \text{ Mpc}$), which are explained by the modifications of the CPDF due to the noise (see text for details). The luminosity of the quasars and the parameters Γ_{12} and γ are identical in the analysis and the generation of Mock spectra (i.e. $L = 5.4 \times 10^{31} \text{ h}^{-2} \text{ erg s}^{-1} \text{ Hz}^{-1}$; $\Gamma_{12} = 1$; $\gamma = 1.5$).

Therefore, the real value of Γ_{12} may be recovered if the density field is uniform.

However, at a distance lower than $3 \text{ h}^{-1} \text{ Mpc}$, a tendency towards overdensity together with a symmetric increase of errors is apparent. The reason is the following. When the ionizing flux from the quasar is high (close to the quasar), the optical depth in most of the pixels is below τ_{min} (see Fig. 4). Then, the modelled (censored) cumulative function (computed from the CPDF in the IGM) is everywhere equal to 1. As for the CPDF measured directly in the spectra, there will always be a fraction of the pixels above τ_{min} due to the noise (this fraction mostly depends on the signal to noise ratio). Therefore, the KS distance between theoretical and measured CPDFs will have a maximum probability at a value larger than 0. This is not the case far away from the quasar, where the theoretical CPDF, for the best-fitting value of $\rho/\langle\rho\rangle$, is the mean of all measured CPDFs. Although most of this effect is included in the function $P_{\text{KS}}(\rho/\langle\rho\rangle)$, this asymmetry will favour a value of $\rho/\langle\rho\rangle$ higher than 1. Besides, a lower $\rho/\langle\rho\rangle$, which is a larger underdensity, will not modify the theoretical CPDF, as long as τ is everywhere lower than τ_{min} . This explains the large error toward low $\rho/\langle\rho\rangle$ for $r \lesssim 10 \text{ h}^{-1} \text{ Mpc}$.

4.4 Recovery of a density structure

The issue at small distances discussed above should be less important if an overdensity is present close to the quasar. Indeed, $\bar{\tau}$ will then remain above τ_{min} at lower distances. We have checked this effect by adding a unique density structure (directly to τ , so in velocity space) in all spectra with the shape $\rho(r)/\langle\rho\rangle = 1 +$

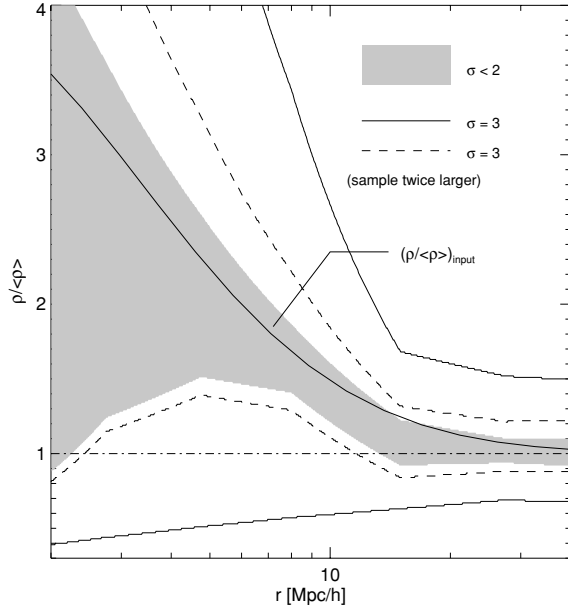


Figure 6. Recovered density structure versus luminosity distance from the analysis of mock LP spectra with an additional input density structure close to the quasar, $(\rho/\langle\rho\rangle)_{\text{input}}$. We assume $L = 5.4 \times 10^{31} h^{-2} \text{ erg s}^{-1} \text{ Hz}^{-1}$, $\Gamma_{12} = 1$ and $\gamma = 1.5$. The 2σ and 3σ confidence levels are indicated as grey region and solid lines, respectively. The 3σ confidence level is also indicated for a sample twice as large as the LP sample (dashed lines).

$3 \exp[-\log(r)]^2/0.6$ (equation 8). We will show in Section 5 that, using this specific structure, the observed evolution of optical depth percentiles is well fitted by the evolution in mock LP spectra (Fig. 9). This input structure is indicated with a solid line in Fig. 6. The 2σ and 3σ confidence levels for the recovered density structure are shown in Fig. 6. It is again consistent with the input structure. As an exercise, the analysis has been repeated with twice as many quasars (i.e. 24). The corresponding contours of the 3σ rejection level are shown with dashed lines in Fig. 6. The constraint is more stringent and still in agreement with the input structure. As expected, the bias is no longer present. Although this result is encouraging, one must remember that the same luminosity and density structure are used for all quasars, which would obviously not be the case in a real and larger sample.

We have shown in two different cases, with a uniform and with an enhanced density, that our analysis does recover the input structure. We now concentrate on the estimation of errors.

4.5 Validation of error estimates

The analysis of one sample (of similar properties as the LP sample) provides us with a probability distribution for the recovered density structure. To validate the estimation of errors, we generate and analyse 50 different samples of mock spectra. In Fig. 7, the results at different radii are reproduced in each panel. For each radius, the range of most probable values of $\rho/\langle\rho\rangle$ obtained for each sample is indicated by a thin horizontal line, while a specific probability distribution corresponding to one sample is shown. This procedure is carried out in the case of an additional density enhancement (Fig. 6). The best-fitting value from different realizations does always fall within the 3σ rejection level estimated from a single sample. The same validation has been performed without additional density structure. The conclusion is the same, although the bias dis-

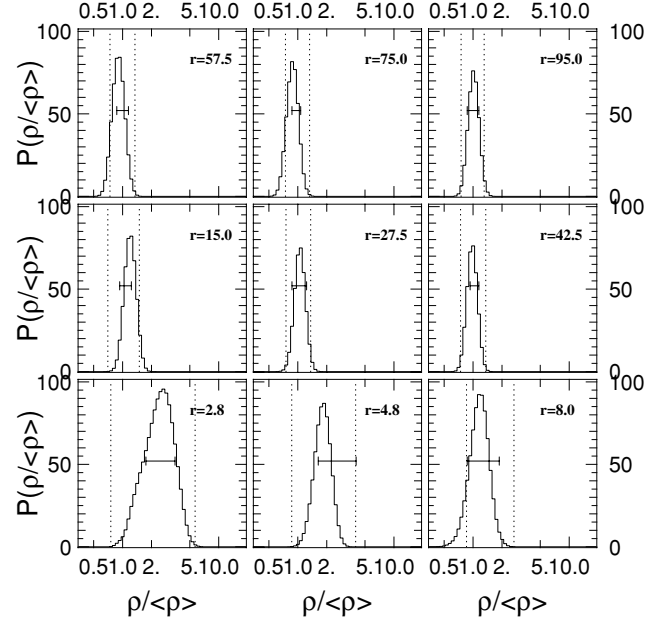


Figure 7. Validation of the estimation of errors in the recovered density structure from mock spectra, with an additional density enhancement (Fig. 6). The probability distribution of $\rho/\langle\rho\rangle$ obtained at different radii and with one sample is shown as a histogram in the different panels. The corresponding radius (luminosity distance in h^{-1} Mpc) is indicated and increases from left to right and bottom to top. The range of most probable values of $\rho/\langle\rho\rangle$ obtained from 50 different samples is indicated as a horizontal line. Each estimation of the most probable value stands between the 3σ rejection level (vertical dotted lines).

cussed above implies that the distribution at low radius is extended toward lower values while the best-fitting value is shifted toward higher values.

Our analysis has been successfully tested with a numerical simulation, for the most probable result as well as the estimation of errors. We may now turn to the analysis of the ESO-VLT LP.

5 APPLICATION TO THE ESO-VLT LARGE PROGRAMME

In this section, we perform, with the LP quasars, the same sequence of analysis described above. First, we have confirmed that the evolution of the mean transmission $\langle F \rangle$ with z is consistent with previous determinations (e.g. Press, Rybicki & Schneider 1993; Schaye et al. 2003). In particular, this gives confidence in the continuum fitting procedure.

Then, we compute the evolution of optical depth with redshift, displayed in Fig. 8 (upper panel). It is stronger than in the mock spectra and seems to favour $\alpha = 6$, when fitted with $\tau_0(z) \propto (1 + z)^\alpha$. However, a slope of 4.5 is allowed within a 3σ confidence level. More importantly, our results are not modified, within the statistical errors, whether we use $\alpha = 4.5$ or the actual fit. The CPDF of the scaled optical depth is shown in Fig. 8 (bottom panel) with the best-fitting result for $\tau_0(z)$. Observations are also consistent with the assumption that the shape of the CPDF does not evolve from $z = 3.2$ to $z = 2.2$.

Once the evolution with redshift is removed, the scaled optical depth CPDFs are computed within different bins in distance to the quasar. The 1σ statistical contours (from a bootstrap resampling) of the evolution of different percentiles are shown in Fig. 9 (grey

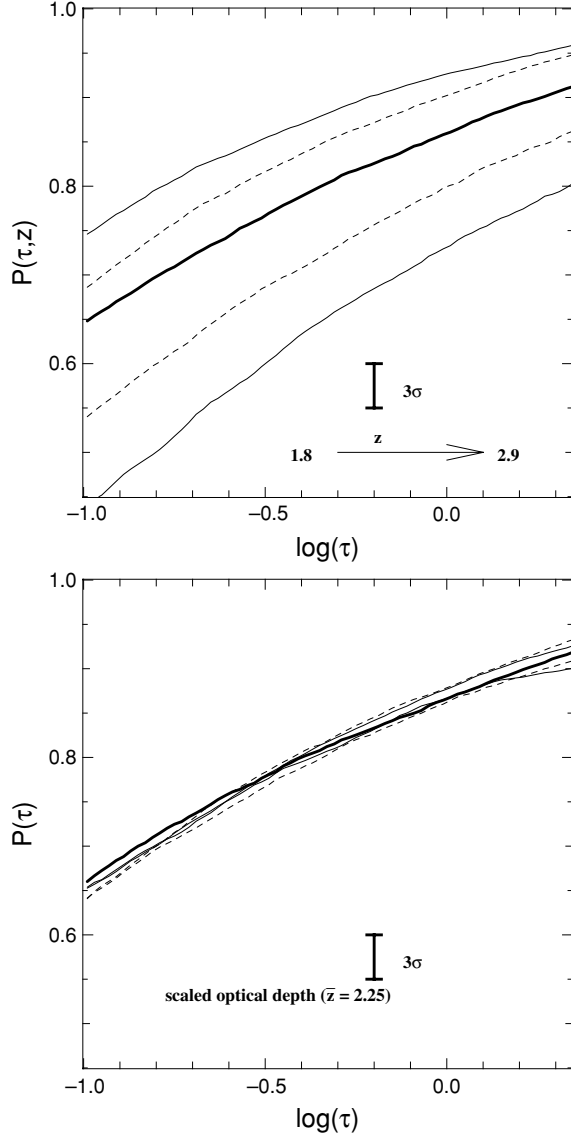


Figure 8. Evolution with redshift of the CPDF of the optical depth, from LP spectra. Notations are the same as in Fig. 3. Top panel: cumulative distributions in five bins in redshifts centred on $z = 1.8, 2.0, 2.25, 2.5$ and 2.95 (left to right, with alternate solid and dashed lines). Bottom panel: same distributions but after scaling each curve to the CPDF at $z = 2.25$ (thick curve in both panels) by a redshift-dependent scaling factor $\tau \rightarrow \tau/\tau_0(z)$.

regions in each panel). We note here that the different percentiles are scaled roughly by the same amount at any given radius (when the lowest contour of τ is larger than the minimum value, i.e. the lower dotted line). This corresponds to the fact that the shape of the CPDF is conserved when one gets closer to the quasar (at the level of accuracy of our sample). This gives confidence in our main assumption that a simple scaling of the reference optical depth is sufficient.

In order to recover the density structure, values of Γ_{12} and γ have to be fixed first. As mentioned earlier, the expected value of γ is between 1 and 1.5 and we use $\gamma = 1.5$ in most of our analysis. The value of Γ_{12} is between 0.3 and 3 (aside from measurements from standard proximity effect analysis), and we use $\Gamma_{12} = 1$. In the previous section, the mean evolution of optical depth percentiles was computed in mock LP spectra without additional density structure

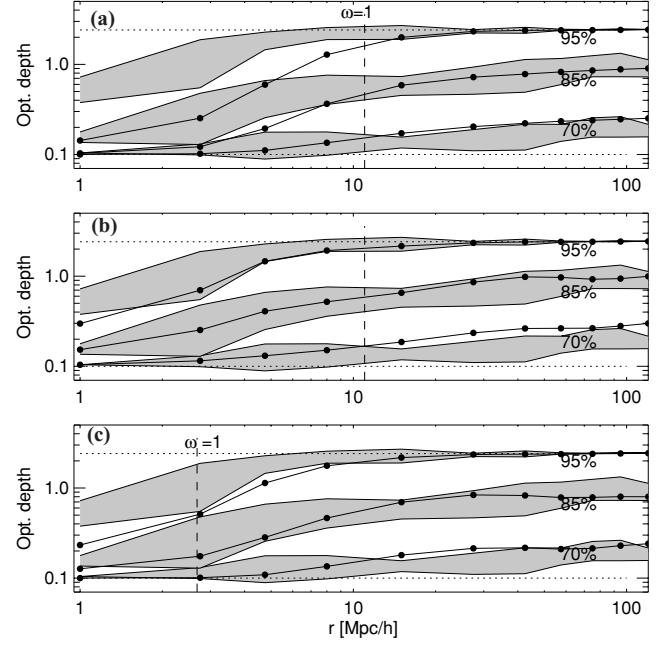


Figure 9. Evolution of different percentiles (95, 85 and 70 per cent) of the distribution of scaled optical depth ($z = 2.25$) with luminosity distance to the background quasar. The 1σ statistical contours corresponding to the LP spectra (with bootstrap resampling) are represented with grey regions in each panel. The position where $\omega = 1$ (dashed line) is computed assuming $\Gamma_{12} = 1$ in (a) and (b), and $\Gamma_{12} = 3.0$ in (c). For comparison, the mean evolution of the same percentiles in mock LP spectra is shown (with solid lines and circles) assuming either $\Gamma_{12} = 1$ and $\rho/\langle\rho\rangle = 1$ (Fig. 4a); $\Gamma_{12} = 1$ and the input density structure shown in Fig. 6(b) or $\Gamma_{12} = 3$ and $\rho/\langle\rho\rangle = 1$ (c). A larger ionization rate or a density enhancement are required to reproduce the observations. Those two cases cannot be distinguished within our analysis.

and using $\Gamma_{12} = 1$ (see Fig. 4). It is overplotted for comparison in Fig. 9(a). In the data, there is no clear change in the percentiles at a radius where $\omega = 1$ (for $\Gamma_{12} = 1$) and even at the lowest radii considered here, the highest percentiles do not reach the minimum optical depth. In contrast, the presence of the ionizing photons from the QSO already strongly affects the optical depth percentiles in mock spectra. Thus, the addition of a density structure is required to counterbalance the increase of the ionization rate. This is shown in Fig. 9(b) where we overplot the evolution of optical depth percentiles in mock spectra including a density structure around the quasar, as described in Section 4.4 (Fig. 6). This provides then a better fit to the observed evolution. The probability distribution of $\rho/\langle\rho\rangle$ associated with the LP QSOs is directly recovered through the procedure described in Section 3. The 2σ confidence region is then displayed in Fig. 10, again for $\Gamma_{12} = 1$ and $\gamma = 1.5$ (Fig. 10b, grey region). A uniform density is rejected at the 2σ level for $r \lesssim 10 h^{-1}$ Mpc proper.

This recovered profile can then be compared to the expected density profile from simulation. For this purpose, we have used the Millennium simulation (Springel et al., in preparation). This dark matter only simulation evolved 2160^3 particles in a box of size $500 h^{-1}$ Mpc, and has $\Omega_m = 0.25$ and $\sigma_8 = 0.9$. Because the LP quasars are very luminous, we extract the averaged density profile around the most massive halo at redshift $z = 2$ in the simulation. The profile, smoothed over $2.5 h^{-1}$ Mpc, is shown as diamonds in Fig. 10. The similarity is encouraging, in particular the fact that both profiles start to increase at the same radius $\simeq 10 h^{-1}$ Mpc.

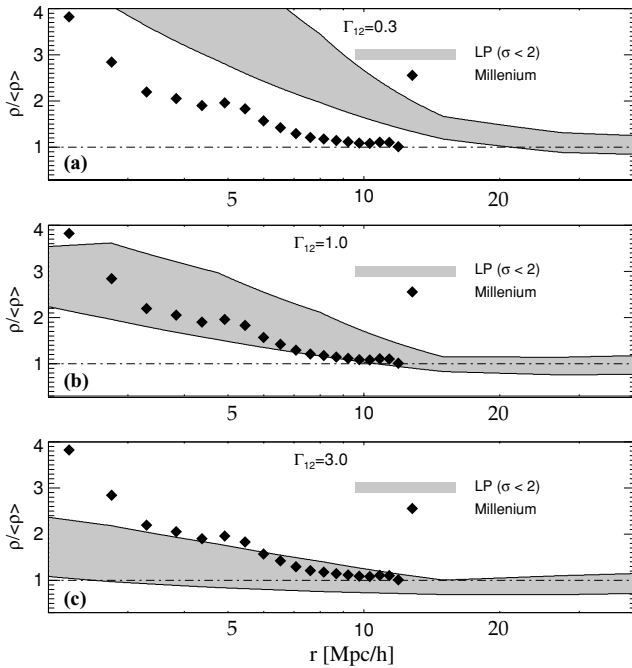


Figure 10. Recovered density structure versus luminosity distance to the background quasar from the analysis of the proximity effect in the LP sample. The density structure, $\rho(r)/\langle\rho\rangle$, is recovered within different bins in distance to the background quasar, from the evolution of the optical depth distribution in the vicinity of the quasar, as compared to the distribution in the IGM. Because the optical depth is a function of the density, the temperature and the amplitude of the ionizing flux, the resulting density structure depends on the slope of the temperature–density relation, γ , and on the amplitude of the background ionizing flux (defined by the parameter Γ_{12}). The value of γ is fixed to 1.5 because uncertainties in it are small enough to have little influence on the result. The 2σ contours of the recovered density structure are shown for $\Gamma_{12} = 0.3$ (a), $\Gamma_{12} = 1$ (b) and $\Gamma_{12} = 3$ (c). A value of $\Gamma_{12} \simeq 1$ is favoured to recover the density enhancement derived around the most massive halo at redshift $z = 2$ in the Millennium simulation (Springel et al., in preparation), which is overplotted in each panel with diamonds.

The effect of varying Γ_{12} and γ is investigated next. It is reasonable to assume that γ is within 1 and 1.5 (see equation 2). Because we actually recover $(\rho/\langle\rho\rangle)^{2-0.7(\gamma-1)}$, varying γ only scales $\rho/\langle\rho\rangle$ in a logarithmic plot. The effect is negligible compared to statistical errors. As for Γ_{12} , we have shown in Section 3 that, for $r \lesssim r_L$, $\rho/\langle\rho\rangle$ is proportional to $(1/\Gamma_{12})^{1+\beta}$. Therefore, the observed optical depth percentiles evolution could also be reproduced in mock spectra with a larger value of Γ_{12} , which decreases the influence of the quasar ionizing flux (the radius where $\omega = 1$ is shifted towards lower distance). The same quality of fit in Fig. 9(c) is indeed obtained with the evolution of optical depth percentiles in mock spectra without density structure but with a larger value of Γ_{12} (3 instead of 1). Similarly, the 2σ confidence region of $\rho/\langle\rho\rangle$ is shown for $\Gamma_{12} = 3$ in Fig. 10(c). The recovered density structure is reduced, and a uniform density can be rejected at the 2σ level for $r \lesssim 2 h^{-1}$ Mpc only. Yet, this may as well be explained by the systematic bias in the recovered structure at small distances (Fig. 5). Higher values of Γ_{12} would result in an underdensity at small distances. Conversely, a lower value of Γ_{12} enhances the recovered density structure, which is demonstrated for $\Gamma_{12} = 0.3$ in Fig. 10(a).

One may then ask the question of which value of Γ_{12} will allow the observation to be consistent with a uniform density $\rho/\langle\rho\rangle = 1$. This corresponds to the standard proximity effect applied to optical

depth statistics. If one requires that a uniform density is not rejected at more than 2σ , within each bin in distance, Γ_{12} is constrained to be within the range 3.6–15. This is consistent with the range of estimates obtained from standard proximity effect analysis using line counting statistics ($\Gamma_{12} \simeq 1.5$ –9). We could also assume the density profile based on the Millennium simulation to recover Γ_{12} . In this case, Fig. 10 shows that $0.3 < \Gamma_{12} \lesssim 3$.

6 CONCLUSION

In this paper we have presented a method to probe the density structure around quasars, using a new analysis of the proximity effect in the absorption spectra of quasars. In the vicinity of the quasar, the additional ionizing photons increase the total ionizing rate, which decreases the Lyman α absorption. Simultaneously, an increase of the density around the quasar (as expected from biased galaxy formation) would increase the absorption. Both effects are better probed with the optical depth than directly with the flux. Our method also avoids fitting the individual absorption lines, and directly uses the cumulative distribution of Lyman α optical depths observed in each pixel. We then model the change of this distribution under modification of the density field and the amplitude of the ionizing rate, Γ_{12} . Our method therefore allows us, in principle, to estimate the density enhancement around host galaxy of quasars, once Γ_{12} is fixed by some other method.

We first use an LCDM high-resolution simulation to validate our method. The information on Γ_{12} and density field is accurately recovered. This gives us confidence to perform our analysis on the real data. We then use the spectra of 12 quasars with highest luminosity at $2.2 < z < 3.3$ from the ESO–VLT LP.

Our method has revealed the presence of an overdensity for $2 \lesssim r \lesssim 10 h^{-1}$ Mpc proper, assuming $\Gamma_{12} < 3$. We have shown that it is consistent with a density profile around the most massive halo at redshift $z = 2$ in the Millennium simulation for $\Gamma_{12} = 1$ (Fig. 10). In the future, a similar analysis should be carried out with a larger sample of spectra, covering different redshift and luminosity ranges. Together with synthetic density profiles computed around haloes of different mass in a large simulation such as the Millennium simulation, this will be very useful to understand better the relation between the environment of the quasar and its host galaxy, and their evolution with redshift. New constraints could also be put on the mass–luminosity relation.

Without knowledge of Γ_{12} , and due to the limited statistics, we could not discard a uniform density profile. Indeed, consistently with standard proximity effect analysis, observations are also modelled without density enhancement, assuming a higher value of Γ_{12} . Yet, due to the specific scaling of the density profile with Γ_{12} , a larger statistics could already allow us to distinguish between different type of profiles, from a simple power law to the existence of alternate shells corresponding to overdensity and underdensity regions. This would be valuable to test the presence of winds, or other specific feedback effects. Thus, it is important to confirm our tentative finding of density enhancement around QSOs (for $\Gamma_{12} < 3$) at high significant level using a bigger sample.

Another application of this analysis concerns the transverse proximity effect. The modelling of the observations obtained with LBGs or quasars has been performed either with simulations (Croft 2004; Maselli et al. 2004) or an analytical model for the density (Schirber et al. 2004). These works could not reproduce the amplitude of the observed effect with normal properties of the quasar, such as anisotropy of the beaming and variability. Combining the constraints on the optical depth evolution along and transverse to

the line of sight could be a way to disentangle the different parameters, that is the density structure, Γ_{12} and the properties of the quasar.

ACKNOWLEDGMENTS

We thank B. Aracil for the reduction and the continuum fitting of the data, and J. Miralda-Escudé for useful comments.

We thank E. Thiébaud, and D. Munro for freely distributing his YORICK programming language (available at <ftp://ftp-icf.llnl.gov/pub/Yorick>), which we used to implement our analysis.

ER was supported by a grant ‘Lavoisier’ from the French Foreign Office. HC thanks CSIR, India for the grant award No. 9/545(18)/2KI/EMR-I and CNRS/IAP for the hospitality. RS and PPJ gratefully acknowledge support from the Indo–French Centre for the Promotion of Advanced Research (Centre Franco–Indien pour la Promotion de la Recherche Avancée) under contract No. 3004-3. TT and PPJ acknowledge support from the European RTN program ‘The Physics of the Intergalactic Medium’. TT thanks the UK Particle Physics and Astronomy Research Council (PPARC) for the award of an Advanced Fellowship, and the Kavli institute at the University of Santa Barbara for hospitality. TT thanks IUCAA for hospitality and the Royal Society for the travel grant to India. Research was conducted in cooperation with Silicon Graphics/Cray Research utilizing the Origin supercomputer at the Department of Applied Mathematics and Theoretical Physics (DAMTP), Cambridge. This research was supported in part by the National Science Foundation under Grant No. PHY99-07949.

REFERENCES

- Adelberger K., Steidel C., Shapley A., Pettini M., 2003, *ApJ*, 584, 45
- Aguirre A., Schaye J., Theuns T., 2002, *ApJ*, 576, 1
- Aracil B., Petitjean P., Pichon C., Bergeron J., 2004, *A&A*, 419, 811
- Bajtlik S., Duncan R., Ostriker J., 1988, *ApJ*, 327, 570
- Bechtold J. B., 1994, *ApJS*, 91, 1
- Bechtold J., Dobrzycki A., Wilden B., Morita M., Scott J., Dobrzycka D., Tran K., Aldcroft T. L., 2002, *ApJS*, 140, 143
- Bi H., 1993, *ApJ*, 405, 479
- Bi H., Davidsen A. F., 1997, *ApJ*, 479, 523
- Bolton J. S., Haehnelt M. G., Viel M., Springel V., 2005, *MNRAS*, 357, 1178
- Bruscoli M., Ferrara A., Marri S., Schneider R., Maselli A., Rollinde E., Aracil B., 2003, *MNRAS*, 343, 41
- Carswell R. F., Whelan J., Smith M., Boksenberg A., Tytler D., 1982, *MNRAS*, 198, 91
- Cen R., Miralda-Escudé J., Ostriker J. P., Rauch M., 1994, *ApJ*, 437, 9
- Chand H., Srianand R., Petitjean P., Aracil B., 2004, *A&A*, 417, 853
- Choudhury T., Srianand R., Padmanabhan T., 2001a, *ApJ*, 559, 29
- Choudhury T., Padmanabhan T., Srianand R., 2001b, *MNRAS*, 322, 561
- Cooke A. J., Espey B., Carswell R. F., 1997, *MNRAS*, 284, 552
- Couchman H. M. P., 1991, *ApJ*, 368, L23
- Couchman H. M. P., Thomas P. A., Pearce F. R., 1995, *ApJ*, 452, 797
- Cowie L. L., Songaila A., 1998, *Nat*, 394, 44
- Cristiani S., Vio R., 1990, *A&A*, 227, 385
- Cristiani S., D’Odorico S., Fontana A., Giallongo E., Savaglio S., 1995, *MNRAS*, 273, 1016
- Croft R., 2004, *ApJ*, 610, 642
- Croft R., Weinberg D., Bolte M., Burles S., Hernquist L., Katz N., Kirkman D., Tytler D., 2002, *ApJ*, 581, 20
- Desjacques V., Nusser A., Haehnelt M. G., Stoehr F., 2004, *MNRAS*, 350, 879
- Efstathiou G., Schaye J., Theuns T., 2000, *Phil. Trans. R. Soc. London A*, 358, 2049
- Espey B. R., Carswell R. F., Bailey J. A., Smith M. G., Ward M. J., 1989, *ApJ*, 342, 666
- Fan X., Tytler D., 1994, *ApJS*, 94, 17
- Fardal M. A., Giroux M. L., Shull J. M., 1998, *AJ*, 115, 2206
- Fernandez-Soto A., Barcons X., Carballo R., Webb J. K., 1995, *MNRAS*, 277, 235
- Francis P. J., 1993, *ApJ*, 407, 519
- Giallongo E., Cristiani S., D’Odorico S., Fontana A., Savaglio S., 1996, *ApJ*, 466, 46
- Gingold R. A., Monaghan J. J., 1977, *MNRAS*, 181, 375
- Giroux M. L., Shapiro P. R., 1996, *ApJS*, 102, 191
- Gunn J. E., Peterson B. A., 1965, *ApJ*, 142, 1633
- Haardt F., Madau P., 1996, *ApJ*, 461, 20
- Haardt F., Madau P., 2001, in Neumann D. M., Van J. T. T., eds, *Proc. XXXVI Rencontres de Moriond (astro-ph/0106018)*
- Haehnelt M. G., Madau P., Kudritzki R., Haardt F., 2001, *ApJ*, 549, L151
- Häring N., Rix H. W., 2004, *ApJ*, 604, 89
- Hernquist L., Katz N., Weinberg D. H., 1996, *ApJ*, 457, 51
- Hockney R. W., Eastwood J. W., 1981, *Computer Simulation Using Particles*. McGraw-Hill, New York
- Hui L., 1999, *ApJ*, 516, 519
- Hui L., Gnedin N. Y., 1997, *MNRAS*, 292, 27
- Hui L., Gnedin N. Y., Zhang Y., 1997, *ApJ*, 486, 599
- Hui L., Haiman Z., Zaldarriaga M., Alexander T., 2002, *ApJ*, 564, 525
- Kulkarni V. P., Fall S. M., 1993, *ApJ*, 413, 63
- Kollmeier J. A., Weinberg D. H., Davé R., Katz N., 2003, *ApJ*, 594, 75
- Liske J., Williger G. M., 2001, *MNRAS*, 328, 653
- Loeb A., Eisenstein D., 1995, *ApJ*, 448, 17
- Lu L., Wolfe A. M., Turnshek D. A., 1991, *ApJ*, 367, 19
- Lu L., Sargent W. L. W., Womble D. S., Takada-Hidai M., 1996, *ApJ*, 472, 509
- Lucy L. B., 1977, *AJ*, 82, 1013
- McDonald P., 2003, *ApJ*, 583, 34
- McDonald P., Miralda-Escudé J., 2001, *ApJ*, 549, L11
- McDonald P., Miralda-Escudé J., 2003, *ApJ*, 595, L67
- Machacek M. E., Bryan G. L., Meiksin A., Anninos P., Thayer D., Norman M., Zhang Y., 2000, *ApJ*, 532, 118
- Magorrian J. et al., 1998, *AJ*, 115, 2285
- Marconi A., Hunt L. K., 2003, *ApJ*, 589, L21
- Maselli A., Ferrara A., Bruscoli M., Marri S., Schneider R., 2004, *MNRAS*, 350, 21
- Miralda-Escudé J., Cen R., Ostriker J. P., Rauch M., 1996, *ApJ*, 471, 582
- Miralda-Escudé J., Haehnelt M., Rees J. R., 2000, *ApJ*, 530, 1
- Mueckert J. P., Petitjean P., Kates R. E., Riediger R., 1996, *A&A*, 308, 17
- Murdoch H. S., Hunstead R. W., Pettini M., Blades J. C., 1986, *ApJ*, 309, 19
- Nusser A., Haehnelt M., 1999, *MNRAS*, 303, 179
- Phillipps S., Horleston N. J., White A. C., 2002, *MNRAS*, 336, 587
- Pichon C., Vergely J. L., Rollinde E., Colombi S., Petitjean P., 2001, *MNRAS*, 326, 597
- Press W. H., Rybicki G. B., Scheiber D. P., 1993, *ApJ*, 414, 64
- Rauch M. et al., 1997, *ApJ*, 489, 7
- Rollinde E., Petitjean P., Pichon C., 2001, *A&A*, 376, 28
- Rollinde E., Petitjean P., Pichon C., Colombi S., Aracil B., D’Odorico V., Haehnelt M. G., 2003, *MNRAS*, 341, 1279
- Savage B. D., Sembach K. R., 1991, *ApJ*, 379, 245
- Schaye J., 2001, *ApJ*, 559, 507
- Schaye J., Theuns T., Leonard A., Efstathiou G., 1999, *MNRAS*, 310, 57
- Schaye J., Theuns T., Rauch M., Efstathiou G., Sargent W. L. W., 2000, *MNRAS*, 318, 817
- Schaye J., Aguirre A., Kim T., Theuns T., Rauch M., Sargent W. L. W., 2003, *ApJ*, 596, 768
- Schirber M., Miralda-Escudé J., McDonald P., 2004, *ApJ*, 610, 105
- Scott J., Bechtold J., Dobrzycki A., Kulkarni V. P., 2000, *ApJS*, 130, 67

- Scott J., Bechtold J., Morita M., Dobrzycki A., Kulkarni V. P., 2002, *ApJ*, 571, 665
- Seljak U., Zaldarriaga M., 1996, *ApJ*, 469, 437
- Srianand R., Khare P., 1996, *MNRAS*, 280, 767
- Steidel C. C., Pettini M., Adelberger K. L., 2001, *ApJ*, 546, 665
- Theuns T., Leonard A., Efstathiou G., Pearce F. R., Thomas P. A., 1998, *MNRAS*, 301, 478
- Theuns T., Bernardi M., Frieman J., Hewett P., Schaye J., Sheth R. K., Subbarao M., 2002, *ApJ*, 574, 111
- Tytler D., Fan X. M., 1992, *ApJS*, 79, 1
- Tytler D. et al., 2004, *ApJ*, 617, 1
- Verner D. A., Ferland G. J., 1996, *ApJS*, 103, 467
- Viel M., Matarrese S., Mo H. J., Theuns T., Haehnelt M. G., 2002a, *MNRAS*, 336, 685
- Viel M., Matarrese S., Mo H. J., Haehnelt M. G., Theuns T., 2002b, *MNRAS*, 329, 848
- Wadsley J., Bond J. R., 1996, *Bull. Am. Astron. Soc.*, 28, 1414
- Weinberg D., 1999, in Banday A. J., Sheth R. K., da Costa L. N., eds, *Proc. ESO/MPQ Conf. Evolution of Large-Scale Structure: From Recombination to Garching*. ESO, Garching, p. 346
- Zhang Y., Anninos P., Norman M. L., 1995, *ApJ*, 453, L57
- Zhang Y., Anninos P., Norman M. L., Meiksin A., 1997, *ApJ*, 485, 496

APPENDIX A: EVOLUTION OF THE PDF WITH REDSHIFT

A key assumption in this paper is that the PDF of the scaled optical depth, $P[\tau(z)/\tau_0(z)]$, varies little with redshift. Here, $\tau_0(z) \propto (1+z)^\alpha$ is a redshift-dependent scaling function, with $\alpha \simeq 4-5$. We have shown in Fig. 3 that this is true for the full optical depth in mock spectra in the range $0.1 \leq \tau/\tau_0 \leq 100$ and in Fig. 8 for the censored, recovered optical depth in the range $0.1 \leq \tau/\tau_0 \leq 2.5$, both at the reference redshift $z = 2.25$. We illustrate in Fig. A1 the limitation of this assumption, by showing the scaled $P(\tau/\tau_0)$ over a larger range. As expected, the PDF becomes wider in its tails as the density field becomes increasingly non-linear at lower redshifts. However, in the range in which we use the PDF, $\tau_{\min} \leq \tau \leq \tau_{\max}$, this dependence is very weak indeed. It also becomes clear from this figure that we cannot reliably determine the shape of the PDF around the maximum for the signal-to-noise ratio in the LP quasars, even at the higher redshifts $z \sim 3$. This is also clear from equation (2): $\tau \sim 0.07 < \tau_{\min}$ at the typical volume-averaged overdensity $\Delta = 1/3$ at $z = 3$, when $\tau_0 \simeq 0.7$. Uncertainties associated with continuum fitting make this part of the PDF uncertain, in addition to these signal-to-noise issues. Note that in our previous analysis we used the recovered optical depth from mock samples, which were continuum-fitted to mimic observed samples. This will strongly affect the shape of the PDF at these low values, and therefore it is not very worthwhile to try to take these lower optical depths into account for the present analysis. In contrast, the mock PDF is uncertain at high τ , where it becomes sensitive to lack of self-shielding and other numerical uncertainties in high-density regions. Given these limitations, can we understand the shape of the optical depth PDF in the intermediate regime?

Miralda-Escudé et al. (2000) provide physical motivation for the following fitting function for the (volume-weighted, real space) overdensity Δ :

$$P(\Delta) d\Delta = A \exp \left[-\frac{(\Delta^{-2/3} - C_0)^2}{2(\delta_0/3)^2} \right] \Delta^{-\beta} d\Delta. \quad (\text{A1})$$

Their table 1 provides values for A , C_0 , δ_0 and β at redshifts $z = 2, 3, 4$ and 6, which they obtained from fitting their numerical

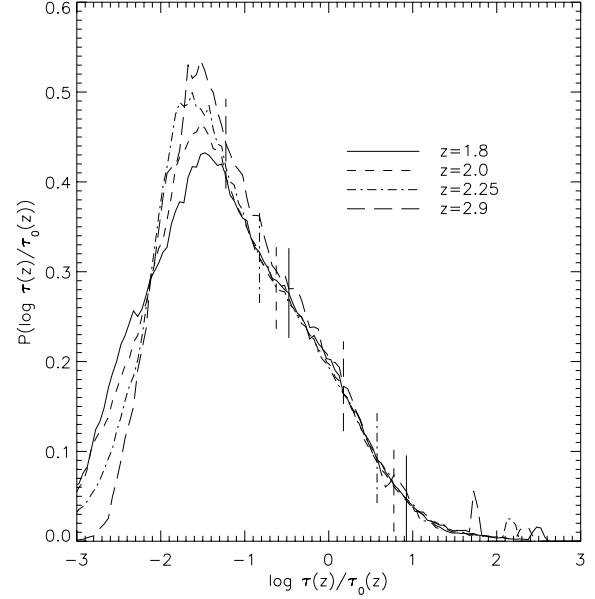


Figure A1. PDF of the true, scaled optical depth, τ/τ_0 , of a large sample (20) of mock LP quasars, in the redshift range $[1.7, 1.9]$, $[1.9, 2.1]$, $[2.15, 2.35]$, $[2.85, 3.05]$. A redshift scaling $\tau_0 \propto (1+z)^5$ is assumed pixel by pixel; the mean redshift is indicated in the panel. Limits in optical depth for the censored PDFs are indicated by thin vertical lines (with corresponding types). The PDFs have a Gaussian shape, with a more extended power-law tail toward low as well as higher optical depths. The shape of the scaled PDF is almost independent of redshift over nearly three decades in $-1 \leq \log(\tau/\tau_0) \leq 2$.

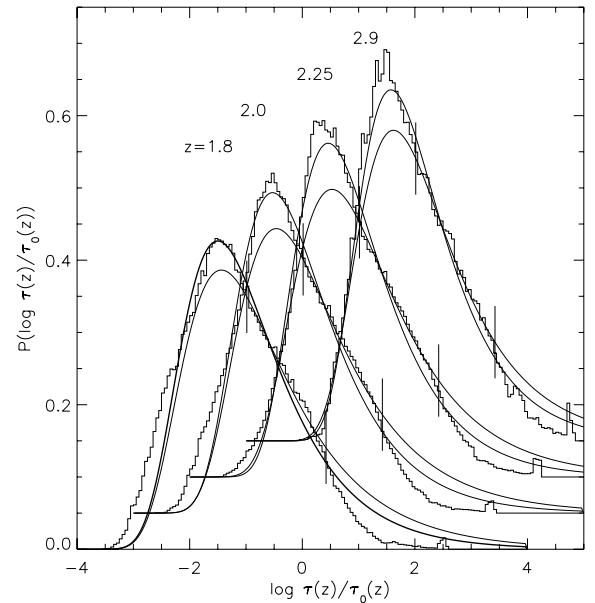


Figure A2. Fits of the form equation (A2) (full lines) to the scaled PDFs shown in Fig. A1, represented here by the histograms. The fits shown by the thin line restrict the fitted region to that of the censored optical depth (vertical lines). Different redshift ranges indicated in the panel are offset vertically and horizontally by 0.05 and 0.1, respectively, for clarity. The fitting function does reasonably well around the maximum and in the power-law tail toward higher τ , but is not able to fit the more non-linear parts at very high and very low τ . The fit to the censored optical depth (thin lines) does not recover well the PDF around the maximum.

Table A1. Best-fitting parameters (equation A2) for the PDF of scaled optical depth, within different redshift bins, restricting the fit to $-2 \leq \log(\tau/\tau_0) \leq 1$ (thin lines in Fig. A2).

z	δ_0	μ	ν
1.8	3.58	1.44	0.46
2.0	3.80	1.46	0.47
2.25	4.09	1.47	0.50
2.9	3.80	1.49	0.52

simulations. The exponent guarantees that the PDF is a Gaussian in $\Delta - 1$ when $C_0 = 1$ and the dispersion $\delta_0 \ll 1$.

We can use this as an Ansatz for the PDF of τ , given the relation equation (2) between Δ and τ . We expect the exponent in the exponential to change $-2/3 \rightarrow -2(1 + \beta)/3$, and $1 + \beta = [0.5, 0.6]$ for $\gamma = [1, 1.6]$, and hence we fit

$$P(x) dx = A \exp \left[-\frac{(x^{-2\nu/3} - C_0)^2}{2(\delta_0/3)^2} \right] (10^x)^{-\mu} dx, \quad (\text{A2})$$

where $x \equiv \log(\tau/\tau_0)$, with free parameters $\nu \approx 1 + \beta$, C_0 , δ_0 and μ , and A is a normalization constant. Restricting the fit to $-2 \leq x \leq 1$, we show the best-fitting PDFs in Fig. A2 and provide the best-fitting parameters in Table A1. The best-fitting value for $C_0 \approx 0$ is kept constant. The dispersion δ_0 differs significantly from the best-fitting one to the density PDF, but the value of the exponent ν is close to expected.

These fits are overlaid on the censored PDF of the observed LP quasar sample in Fig. A3. The good agreement suggests that the mock sample is indeed representative of the observed distribution.

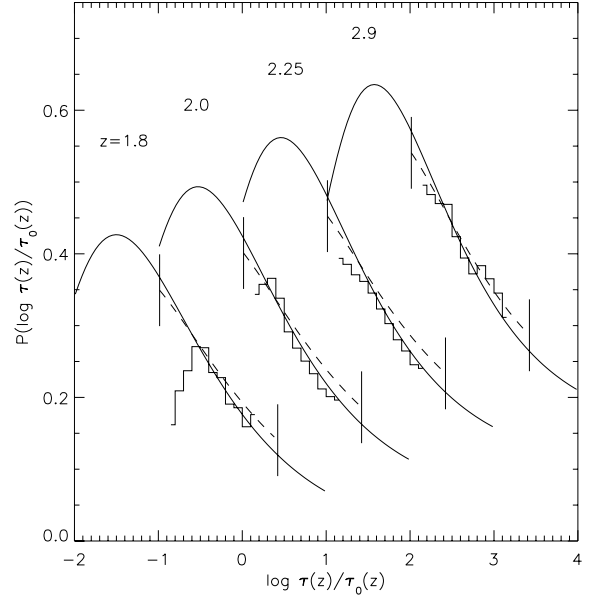


Figure A3. Overlay of the fits to the scaled PDF of the mock sample from Fig. A1 to the (censored) scaled PDF of the LP quasar sample. The same redshift scaling $\tau_0 \propto (1 + z)^5$ is assumed for the LP data. The same redshift range are indicated and shifted as in Fig. A2. The agreement is very good, increasing our confidence that the mock samples are sufficiently realistic for validating our method.

This paper has been typeset from a \LaTeX file prepared by the author.